# Hydrogen Trapping in Laser Powder Bed Fusion 316L Stainless Steel

Polina Metalnikov [1,2], Guy Ben-Hamu [2,*] and Dan Eliezer [1]

1   Department of Material Engineering, Ben-Gurion University of the Negev, Beer-Sheva 84105, Israel
2   Department of Mechanical Engineering, Sami Shamoon College of Engineering, Ashdod 77245, Israel
*   Correspondence: guy@sce.ac.il; Tel.: +972-547787911

**Abstract:** In this study, the hydrogen embrittlement (HE) of 316L stainless steel produced by laser powder bed fusion (L-PBF) was investigated by means of hydrogen trapping. The susceptibility of the material to HE is strongly connected to the interaction of hydrogen atoms with volumetric defects in the material. Trapping hydrogen in those defects affects its availability to critical locations where a hydrogen-induced crack can nucleate. Therefore, it is important to study the characteristics of hydrogen traps to better understand the behavior of the material in the hydrogen environment. The hydrogen was introduced into the material via electrochemical charging, and its interactions with various trapping sites were studied through thermal desorption spectroscopy (TDS). The obtained results were compared to conventionally produced 316L stainless steel, and the correlation between microstructure, characteristics of hydrogen traps, and susceptibility to HE is discussed.

**Keywords:** hydrogen embrittlement; 316L stainless steel; additive manufacturing; hydrogen trapping; thermal desorption spectroscopy

## 1. Introduction

Austenitic stainless steels (ASSs) are characterized by good mechanical properties, excellent formability, toughness, and corrosion resistance, both at low and high temperatures. This is the prevalent family of stainless steel (SS) in terms of usage and number of alloys [1]. ASS, and particularly stable ASS, e.g., 316 and 316L, are also considered to be fairly resistant to hydrogen-induced damage and hydrogen embrittlement (HE), especially compared with ferritic and martensitic SS [1–4]. The enhanced resistance to HE of ASS is usually attributed to the lower diffusivity and higher solubility of hydrogen in the fcc γ-austenite phase [5], as well as to the retarded transformation of γ to strain-induced martensite [6–8].

Nowadays, ASS can be produced by various additive manufacturing (AM) technologies. These technologies possess the unique ability of the production of complex shaped parts in a relatively short time. One of the most common AM processes is laser powder bed fusion (L-PBF). During the L-PBF process, a thin layer of powder is spread on the build platform and then selectively melted by a high-energy laser beam [9–11]. This results in very high cooling rates, and the microstructure of L-PBF ASS, particularly 316L, is reported to consist of relatively fine austenite grains with irregular shape and a metastable cellular sub-grain structure [12–17]. As a result, L-PBF ASS usually presents improved strength and ductility in comparison to conventionally produced counterparts [17–20].

The susceptibility of L-PBF ASS to HE has been studied recently by various researchers [21–24]. In general, hydrogen is reported to have little negative effect on L-PBF ASS. This is attributed to the unique microstructure of the material, produced by L-PBF. For instance, it was proposed by Kong et al. [21] that the fine cellular structure formed in L-PBF 316L SS can restrict the generation of twins, resulting in a lower possibility of martensite transformation during hydrogen charging. The sub-grain boundaries might provide rapid transportation channels for hydrogen atoms, hence increasing the diffusion rate [22]. Melt

pool boundaries can act as hydrogen trapping sites, affecting the hydrogen-enhanced localized plasticity mechanism [23]. In addition, an absence of retained δ-ferrite was observed in L-PBF 316L SS, whereas this phase was present in conventionally produced alloy [24]. According to [24], the presence of δ-ferrite results in the inhomogeneous distribution of alloying elements in the γ-matrix. As a result, austenite stability decreases in the areas near the δ-ferrite particles, enhancing the localized transformation of γ to strain-induced α'-martensite. Higher austenite stability and a lower degree of $\gamma \rightarrow$ martensite transformation indicate the better resistance of L-PBF 316L SS to HE. However, it should be noted that the susceptibility to hydrogen-assisted damage strongly depends on the interactions of hydrogen atoms with defects in the material. These defects can temporarily or permanently trap the hydrogen atoms, thus affecting the hydrogen diffusivity and solubility within the material [25–27]. Moreover, the availability of hydrogen atoms to the critical locations where cracks can be developed is also controlled by hydrogen trapping sites. Therefore, for a better understanding of the behavior of the material in a hydrogen environment, it is important to study the characteristics of hydrogen traps. While there are numerous studies regarding hydrogen trapping in conventionally produced ASS [28–32], to the best of our knowledge, there is a lack of information on this issue about L-PBF ASS.

In our study, we refer to and compare hydrogen trapping and desorption characteristics in 316L SS prepared using L-PBF and conventional cold rolling (CR). The hydrogen was introduced via electrochemical charging at room temperature, and its effect on the microstructure was studied with X-ray diffraction (XRD), and optical and electron microscopy. Thermal desorption spectroscopy (TDS) was used to evaluate the activation energy of various hydrogen traps that exist within the material. The dependence of susceptibility to HE on the characteristics of hydrogen traps and initial microstructure will be discussed.

## 2. Materials and Methods

An L-PBF specimen of 316L SS was made using an SLM 280HL machine (SLM Solutions GmbH, Lübeck, Germany) equipped with a 400 W Yb fiber laser. A metal powder with a particle size between 10 and 45 μm was supplied by SLM Solutions. The process was completed in a protective ultra-high-purity argon atmosphere; the laser power, scan speed and hatch spacing were set to 200 W, 800 mm/s and 120 μm, respectively. After each layer, the scanning direction was rotated by 90°. The microstructure and hydrogen interactions with the L-PBF 316L SS were compared to the conventionally produced cold-rolled (CR) counterpart of 316L SS (ASTM A240/A240M-05 [33]) supplied by Hamatechet M. Felsenstein Ltd. (Haifa, Israel). The chemical compositions of L-PBF and CR 316L SS specimens, as reported by the manufacturer, are presented in Table 1.

**Table 1.** Chemical compositions (wt%) of L-PBF and cold-rolled (CR) 316L SS.

|  | Fe | Cr | Ni | Mo | Mn | Si | P | S | C | N |
|---|---|---|---|---|---|---|---|---|---|---|
| L-PBF | Balance | 17.6 | 12.8 | 2.30 | 1.10 | 0.65 | 0.004 | 0.004 | 0.02 | 0.045 |
| CR | Balance | 16.6 | 10.3 | 2.07 | 1.11 | 0.41 | 0.036 | 0.001 | 0.023 | 0.021 |

Phase identification was made using a Rigaku D/MAX-2000 X-ray diffractometer (XRD) with Cu-Kα radiation with a scanning angle from 40° to 85° and a scanning velocity of 0.02°/s. Microstructure analysis was carried out using a Carl Zeiss Axio Observer A1m optical microscope (OM) and a JEOL JSM-IT100 scanning electron microscope (SEM). The metallographic preparation included polishing up to 0.25 μm and subsequent etching with 10 mL $HNO_3$, 10 mL acetic acid, 15 mL HCl, and 5 drops of glycerol for 2 min [34].

The hydrogen was introduced into the material via electrochemical hydrogen charging in a 0.5 N $H_2SO_4$ water solution. Then, 0.25 g/L of $NaAsO_2$ was added to the electrolyte as poison for hydrogen recombination. Samples were charged at room temperature (RT) with a constant current density of 50 mA/cm$^2$ for 72 h. Afterwards, the samples were stored in liquid nitrogen to avoid hydrogen outgassing.

The interactions of introduced hydrogen with various microstructural defects were investigated by means of thermal desorption spectroscopy (TDS). TDS measurements were carried out with a custom-made thermal desorption system designed and assembled at Ben-Gurion University. The system consists of an ultra-high vacuum chamber, in which the pre-charged specimen is placed in a specimen holder made of oxygen-free high copper. The high vacuum is achieved by a combination of a rotary pump and a turbo-molecular pump. The specimen holder is heated by a coaxial heating coil, and the temperature is measured by two thermocouples located very close to the sample. A quadrupole mass-spectrometer (PrismaPro® QMG 250) was used to measure the amount of desorbed hydrogen and the temperature. In this work, the pre-charged specimens were non-isothermally heated from RT to 600 °C at constant heating rates of 2 °C/min, 4 °C/min and 6 °C/min. The thermodesorption spectra were analyzed with PV MassSpec software using Lee and Lee's model [35]. The working procedure, as described elsewhere [35–37], enables the identification and characterization of various hydrogen traps within the material.

In order to observe the effect of hydrogen desorption on the possible phase transformations within the material, the pre-charged specimens were aged at RT for different time intervals and then examined with XRD, OM and SEM.

## 3. Results

Figure 1 presents the micrographs of the as-received CR and L-PBF 316L SS. The microstructure of the CR specimen, shown in Figure 1a, consists of polygonal-shaped grains with a large amount of deformation twins. On the opposite side, the grains of L-PBF 316L SS present an elongated shape, and they are separated by melt pool boundaries, marked in Figure 1b. High magnification SEM images of Figure 1c,d reveal a metastable cellular sub-grain structure, with cell sizes less than 1 μm. This structure is commonly observed in austenitic SS produced via L-PBF [12–17]. The prevalent phase in both CR and L-PBF specimens is $\gamma$-austenite with an fcc crystal structure, which is manifested by the XRD patterns in Figures 2 and 3 (black line). Additional peaks, observed in the spectra of uncharged CR specimens, belong to $\alpha'$-martensite with a bcc crystal structure. No $\varepsilon$-martensite was observed for L-PBF nor for CR 316L SS in the initial state.

In order to evaluate the hydrogen-induced microstructural changes of 316L SS, an XRD analysis was performed on electrochemically hydrogenated L-PBF and CR specimens. Figure 2 presents the XRD patterns of L-PBF 316L SS after 72 h of hydrogen charging, followed by aging at RT. It can be seen that hydrogenation resulted in a slight expansion of the austenite lattice parameter, manifested by peak shifting to lower 2θ values. Moreover, new reflections were observed after 72 h of hydrogen charging, and they are ascribed to the $\alpha'$-martensite phase. It is interesting to notice that in hydrogenated commercial 316L SS, the peaks of $\alpha'$-martensite appeared only after a prolonged aging time [38]. In our study, as can be seen in Figure 2 that the peaks ascribed to $\alpha'$-martensite appeared immediately after hydrogen charging.

After aging for 24 h, the solute hydrogen was desorbed out of the $\gamma$ phase, manifested by the shift of the reflections towards higher 2θ values. A longer period of aging resulted in the appearance of new peaks, ascribed to the $\varepsilon$-martensite phase. Thus, it can be suggested that during aging, the $\varepsilon$-martensite phase becomes more stable. The same phenomenon was reported for conventionally produced SS [28,39].

The XRD patterns of hydrogenated and aged CR 316L SS (Figure 3) present two interesting observations. First, the effect of hydrogen on the $\gamma$ phase is more pronounced, compared with $\alpha'$-martensite. The reflections of the $\gamma$ phase were shifted to lower 2θ values, indicating lattice expansion due to the solute hydrogen, whereas the peaks of $\alpha'$ remained in their places. A second observation is that $\varepsilon$-martensite precipitated immediately after hydrogen charging. Upon aging, the intensity of both $\alpha'$ and $\varepsilon$ martensite reflections decrease due to the partial dissolution of these phases. However, even after 1 month of aging, they do not disappear completely, implying high stability. Compared with the XRD patterns of L-PBF 316L SS, it is clearly seen that the peak intensities for both $\alpha'$ and $\varepsilon$

martensite phases are higher in the CR specimen. Thus, it can be assumed that L-PBF 316L SS has a lower susceptibility to martensitic transformation during hydrogen charging compared with conventionally produced material. No pseudo-hydride $\gamma^*$ phase was observed in the XRD patterns of either L-PBF or CR 316L SS.
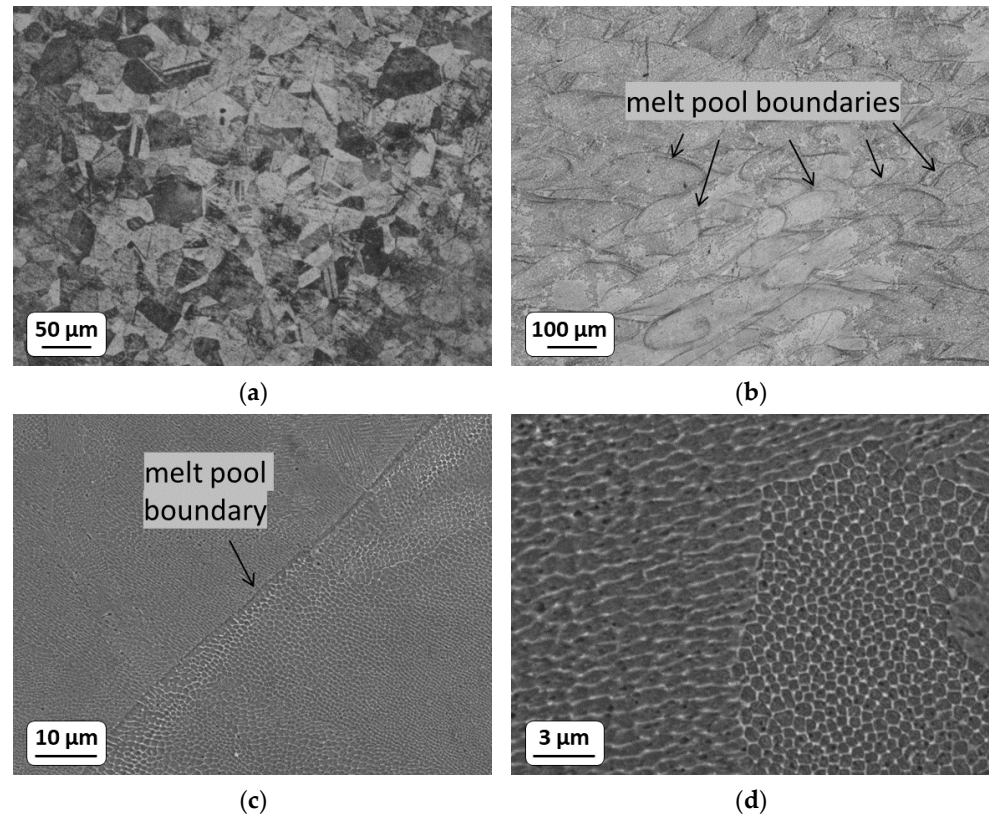


**Figure 1.** OM micrographs in the XZ direction of CR (**a**) and L-PBF (**b**) 316L SS prior to the hydrogen charging. Higher magnification SEM images of L-PBF 316L SS (**c**,**d**).
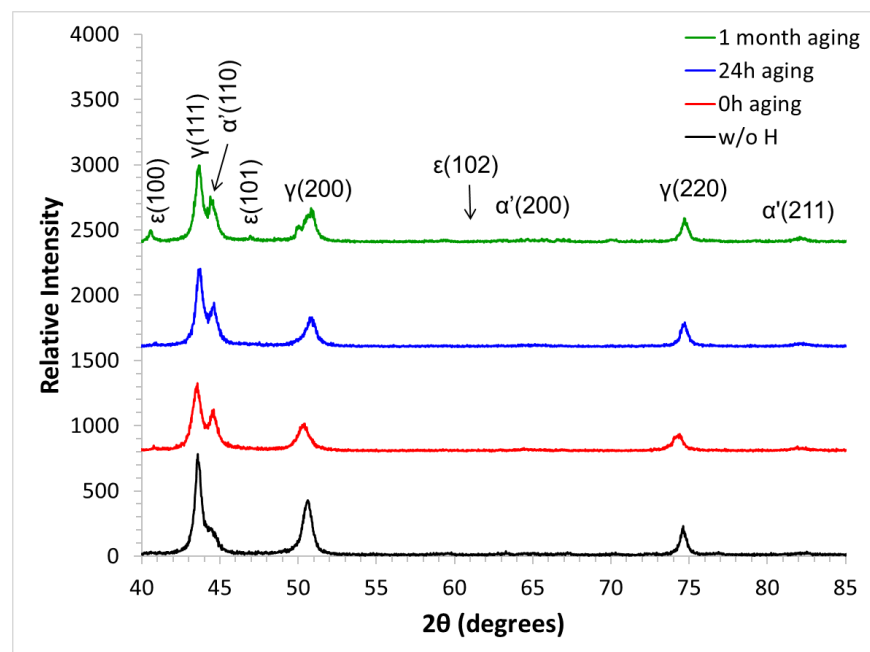


**Figure 2.** XRD patterns of the uncharged and hydrogenated L-PBF 316L SS for 72 h, followed by aging for different time intervals.
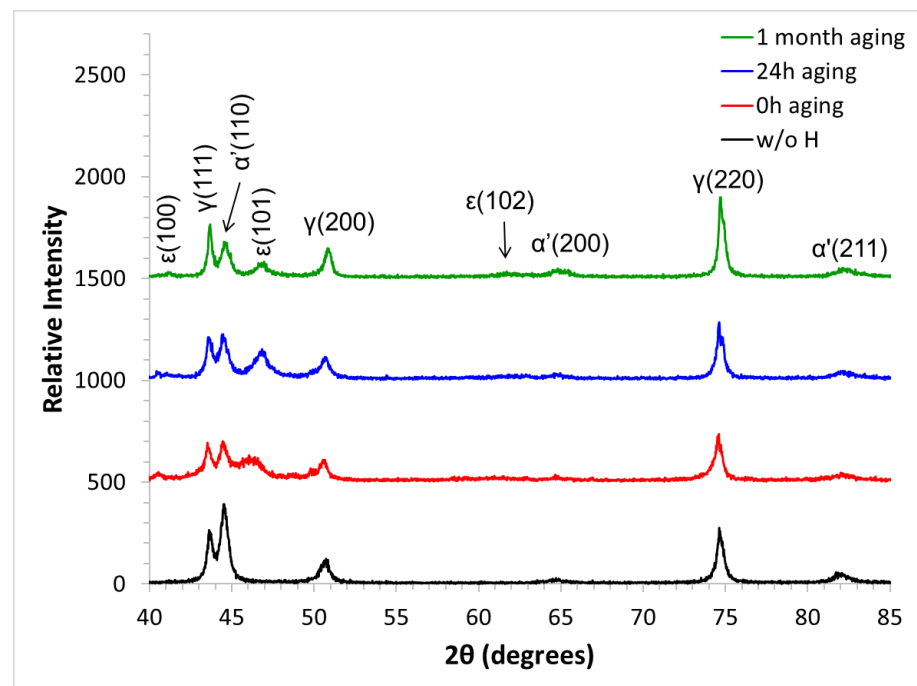
**Figure 3.** XRD patterns of the uncharged and hydrogenated CR 316L SS for 72 h, followed by aging for different time intervals.

No cracks were observed after hydrogen charging, either on the CR or on the L-PBF specimens (see Figure 4). However, hydrogen charging resulted in the appearance of some hydrogen-related microvoids in both specimens. In the CR 316L SS, these microvoids nucleate in the interior of the grain (Figure 4c), whereas in L-PBF 316L SS, the microvoids seem to preferentially nucleate on the melt pool boundaries (Figure 4d).

Hydrogen desorption characteristics in 316L SS were studied using TDS. With this method, we were able to identify different hydrogen traps within the material and to estimate the activation energy, $E_a$, for hydrogen release from each trap. In general, the traps are classified to be reversible ($E_a < 60$ kJ/mol) and irreversible ($E_a \geq 60$ kJ/mol) [40]. The TDS spectra of L-PBF and CR 316L SS (Figures 5a and 6a) present two hydrogen desorption peaks: the main one at relatively low temperatures, and a small peak at higher temperatures. The shape of the TDS spectra is similar to the one obtained for austenitic SS in previous studies for both the conventional type [31,41] and AM [24]. Table 2 summarizes the estimated activation energies of the hydrogen traps for the specimen, calculated from Figures 5b and 6b. The main desorption peak of L-PBF 316L SS presents a relatively low value of activation energy for hydrogen desorption, $28 \pm 4$ kJ/mol, implying the presence of a reversible trap. According to previously published works [28–30,39,42–45], this trap can be ascribed to an elastic stress field around dislocation or second-phase particles ($E_a \sim 0$–20 kJ/mol), or a dislocation core ($E_a \sim 20$–35 kJ/mol). An additional peak is observed at higher temperatures and its activation energy was found to be $62 \pm 5$ kJ/mol. This value can be attributed to an irreversible trap with relatively low activation energy, or a reversible trap with relatively high activation energy. These traps in steels can be $\alpha/\gamma$ interfaces ($E_a \sim 50$–57 kJ/mol [42,46,47]), austenite bulk ($E_a \sim 55$ kJ/mol [43]), high-angle grain boundaries ($E_a \sim 53$–59 kJ/mol [29,48,49]), $\varepsilon/\alpha'$ martensite ($E_a \sim 58$–62 kJ/mol [28]), or $\gamma^*$ pseudo hydride phase ($E_a \sim 63$ kJ/mol [39]).

(**a**)  (**b**)

(**c**)  (**d**)
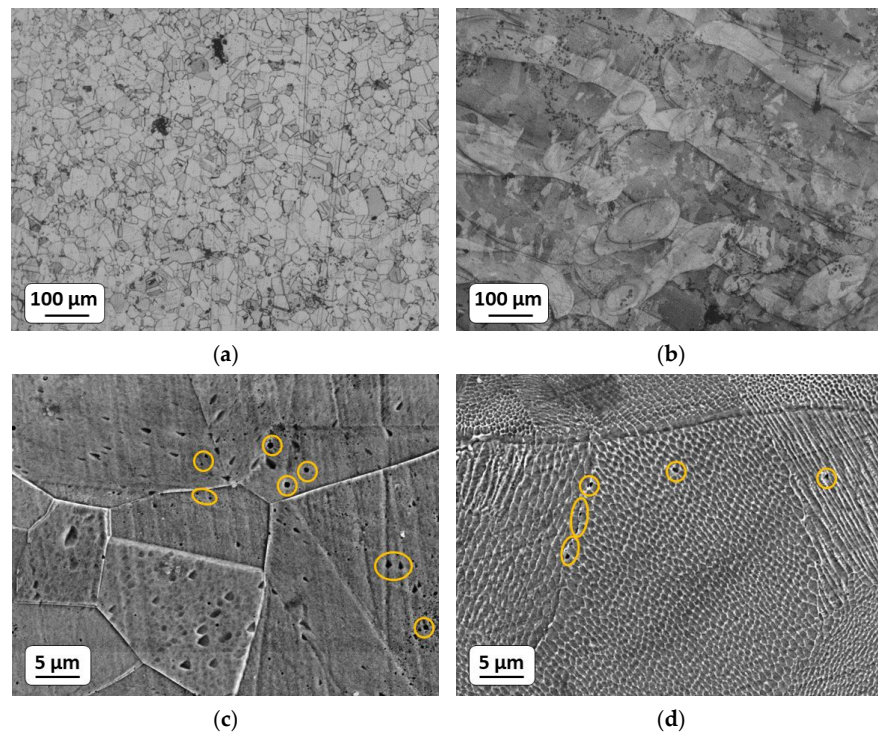
**Figure 4.** OM micrographs of CR (**a**) and L-PBF (**b**) 316L SS after 72h of electrochemical charging, followed by aging at RT. Higher magnification SEM images of CR (**c**) and L-PBF (**d**) 316L SS show the microvoids, marked with yellow circles.
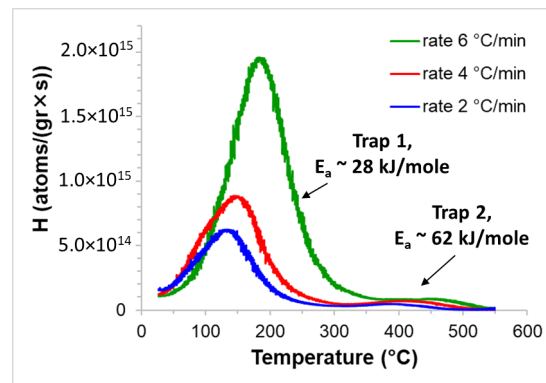


(**a**)
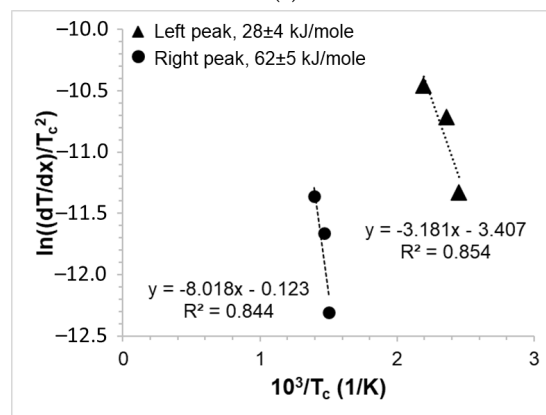


(**b**)

**Figure 5.** TDS spectra of hydrogenated L-PBF 316L SS for 72 h (**a**) and determination of the activation energies for three hydrogen desorption peaks of hydrogenated L-PBF 316L SS (**b**).
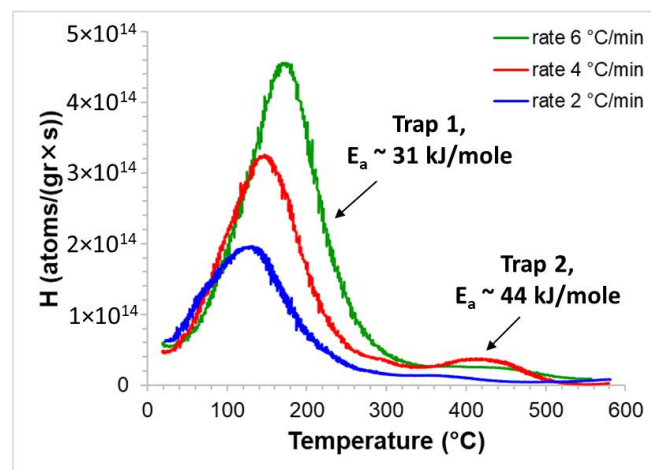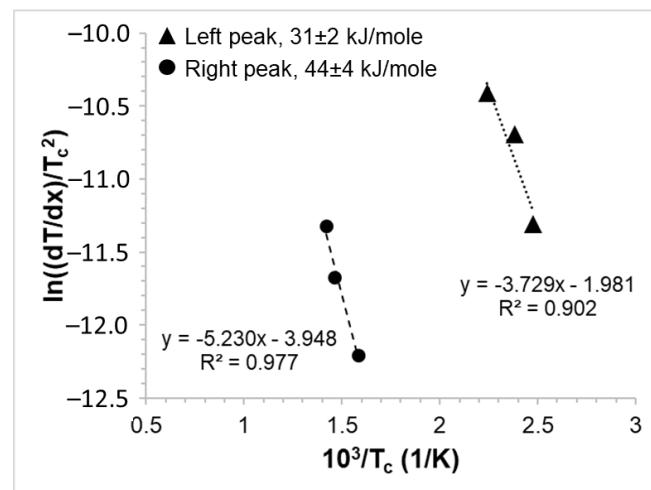
(a)



(b)

**Figure 6.** TDS spectra of hydrogenated CR 316L SS for 72 h (**a**) and determination of the activation energies for three hydrogen desorption peaks of hydrogenated CR 316L SS (**b**).

**Table 2.** Parameters of obtained hydrogen traps in the TDS spectra of L-PBF and CR 316L SS.

| Sample | Temperature Range (°C) | $E_a$ (kJ/mole) |
|--------|------------------------|-----------------|
| L-PBF | ~135–180 | $28 \pm 4$ |
| | ~390–450 | $62 \pm 5$ |
| CR | ~130–170 | $31 \pm 2$ |
| | ~360–430 | $44 \pm 4$ |

Figure 6a presents the TDS spectra of CR 316L SS, and the activation energies calculated from Figure 6b are summarized in Table 2. The value of the activation energy of the main desorption peak is within the error range of the reversible trap in L-PBF 316L SS. Therefore, we can assume that the main hydrogen trap in both materials is the elastic stress field or a dislocation core. The second peak appears at higher temperatures, and its activation energy was found to be $44 \pm 4$ kJ/mol. Since it is lower than 60 kJ/mol, both hydrogen traps of CR 316L SS are reversible. According to the literature, the second trap can be ascribed either to the interstitial diffusion of hydrogen atoms within the γ-matrix ($E_a \sim 40$ kJ/mol [32,47,50]), or to γ grain boundaries ($E_a \sim 37$–43 kJ/mol [28,29,39,51]).

It is interesting to notice that, although CR 316L SS presents a higher amount of martensite phases, it has no irreversible hydrogen traps.

## 4. Discussion

Comparing the L-PBF and CR specimens, we can clearly see that the manufacturing method has a strong impact on the initial microstructure (Figure 1). The L-PBF 316L SS is characterized with an elongated grain structure, implying that new grains epitaxially grow along the building direction from the re-melted zones [52,53]. Furthermore, metastable cellular structure was observed, which is attributed to the thermal contraction during L-PBF processing [14]. According to Gorsse et al. [14], high cooling rates result in a large dislocation density, and the dislocations are rearranged as fine dislocation cells. Kong et al. [17] reported that the morphology of this sub-structure is generally cylindrical, and the growth direction is usually aligned with the direction of the maximum heat flow. Elements such as Cr and Mo are found to segregate to the cellular boundary, as well as nanoparticles of silicates enriched with transition metals [12–17]. It should be noted that the microsegregation of Cr and Mo is not sufficient to stabilize the ferrite phase; thus, usually it is not observed in as-built L-PBF 316L SS [13]. On the other hand, the CR specimen presented a significant amount of $\alpha'$-martensite in the as-received state (Figure 3). The formation of martensite in the CR specimen is related to the induced strains during the cold-rolling processing [54–56].

The electrochemical hydrogen charging of 316L SS results in induced stresses in the $\gamma$-austenite lattice due to the relatively high hydrogen solubility in this phase [46]. In the case of the CR specimen, the effect of hydrogen was more pronounced in the $\gamma$-phase than in $\alpha'$-martensite (Figure 3). This is attributed to the different solubilities of hydrogen in the $\gamma$-fcc and $\alpha'$-bcc phases [5,46]. Same phenomenon was observed in duplex SS [28], where the initial microstructure consisted of $\gamma$-austenite and $\alpha$-ferrite phases. In addition, the partial transformation of austenite to $\alpha'$ and $\varepsilon$ martensite occurred in both specimens. This phase was also found in hydrogen-charged austenitic SS prepared via conventional methods [57], and its presence is attributed to the introduced internal stresses within the material during the hydrogenation. Other studies ascribe the formation of $\alpha'$-martensite to the elastic stresses which appear during hydrogen desorption [28,38,58]. Hydrogen-induced damage was also manifested by the appearance of hydrogen-related microvoids. This kind of microvoid was observed in wrought and AM Ti-6Al-4V after electrochemical hydrogenation [59]. According to [59], the number of the observed microvoids increases with increasing charging time, and they might serve as nucleation sites for hydrogen-induced cracks. Since the transformation to martensite and the appearance of microvoids are more pronounced in conventionally produced CR 316L SS, we can suggest that AM processing might improve the resistance of the material to hydrogen-induced damage.

Moreover, 316L austenitic SS is considered to be fairly resistant to HE, compared with ferritic and martensitic SS [1]. CR processing results in the appearance of strain-induced $\alpha'$, which might increase the sensitivity of the material to HE. This is attributed to a higher diffusion rate of hydrogen in the $\alpha'$-martensite phase, compared with that in $\gamma$ [60,61]. As a result, martensite might act as a short-path for hydrogen atoms to critical cracking locations, hence promoting hydrogen-assisted cracking (HAC) [6–8]. However, it was reported by Zhang et al. [8] and by Buckley and Hardie [62] that $\alpha'$-martensite formed by pre-strain has a negligible effect on the susceptibility of the material to HE. According to [8], only the martensite formed during deformation (after the pre-strain) shows obvious HE. Therefore, it can be suggested that the higher susceptibility of CR 316L SS is not necessarily due to the presence of the $\alpha'$-martensite phase prior to hydrogen charging.

During the hydrogenation, both specimens presented a transformation from $\gamma$ to $\alpha'$ and $\varepsilon$ martensite, which might promote HE. However, it can be clearly seen in Figures 2 and 3 that the amount of hydrogen-induced martensite is higher for the CR specimen, manifested by the higher intensity of their peaks. The $\gamma \rightarrow$ martensite transformation strongly depends on the stability of the $\gamma$-phase. Lower austenite stability results in a higher amount of stress-induced martensite [28,38]. Moreover, it was reported by Rozenak and Eliezer [38,63,64] that high hydrogen concentration decreases the austenite stability and induces $\gamma \rightarrow$ marten-

site transformation. The austenite stability factor depends on the composition of the alloy and can be expressed as [65,66]:

$$S\gamma = Ni + 0.68Cr + 0.55Mn + 0.45Si + 27(C + N) \tag{1}$$

where $S\gamma$ is the austenite stability factor and Ni, Cr, Mn, Si, C and N are the stabilizing elements in weight percentage. Additional parameters which are commonly used to describe austenite stability are $M_{d30}$ temperature and stacking fault energy (SFE). $M_{d30}$ temperature is the lowest temperature where 30% true plastic strain causes 50% of $\gamma \rightarrow \alpha'$-martensite transformation [67,68]. SFE values can predict the tendency of fcc materials towards martensitic transformation [69,70]. Moreover, low SFE values are correlated with higher susceptibility to hydrogen-induced fracture [4,70,71].

Both $M_{d30}$ temperature and SFE depend on the chemical composition of the material, and can be expressed as [72,73]:

$$M_{d30} (^\circ C) = 413 - 462(C + N) - 9.5Ni - 13.7Cr - 8.1Mn - 18.5Mo - 9.2Si \tag{2}$$

$$SFE (mJ/m^2) = -7.1 + 2.8Ni + 0.49Cr + 2.0Mo - 2.0Si + 0.75Mn - 5.7C \tag{3}$$

where Ni, Cr, Mn, Mo, Si, C and N are the stabilizing elements in weight percentage. The obtained parameters are summarized in Table 3.

**Table 3.** Calculated parameters affecting austenite stability of L-PBF and CR 316L SS.

| Sample | L-PBF | CR |
|---|---|---|
| $S_\gamma$ | 27.4 | 23.6 |
| $M_{d30}$ (°C) | −34.8 | 16.3 |
| SFE (mJ/m²) | 39.6 | 33.9 |

As can be seen from Table 3, all the parameters predict higher austenite stability for the L-PBF specimen, compared with CR. In other words, when these two materials are exposed to the same hydrogen charging conditions, L-PBF 316L SS is expected to show less transformation to martensite. Our results are in line with this assumption.

The stability of austenite can be also promoted by the non-equilibrium microstructure of L-PBF 316L SS. It was reported that the cellular sub-grain structure might suppress martensitic transformation during plastic deformation [74] or hydrogen charging [21]. Hong et al. [74] claimed that the fine cellular microstructure and high density of low-angle grain boundaries of L-PBF 316L SS restrict deformation twins and dislocation slip, thus reducing the martensite nucleation sites and increasing the stability of the γ-phase. Kong et al. [21] observed martensite nucleation on the nano-twin boundary in hydrogenated wrought 316L SS and proposed that the fine cellular structure of L-PBF 316L SS can restrict the generation of twins and the further transformation to martensite. Hence, we suggest that suppressed γ → martensite transformation in L-PBF 316L can be attributed to two factors: (i) higher austenite stability, and (ii) cellular sub-grain structure. Lower amounts of hydrogen-induced martensite result in the better resistance of L-PBF 316L SS to HE.

An additional difference between the L-PBF and CR specimens is the characteristics of the hydrogen traps. As was mentioned previously, the traps are classified as reversible and irreversible [40]. Irreversible traps act as hydrogen sinks, whereas reversible traps might act as hydrogen sources within the material and exchange hydrogen with stronger traps [25,75]. Moreover, reversible traps can supply hydrogen atoms to critical cracking locations, where their presence might affect the fracture behavior [25]. Thus, the susceptibility of a material to HE depends not only on the characteristics of the population of hydrogen traps, but also on the competition between reversible and irreversible traps.

Both specimens presented two hydrogen traps, and the values of activation energy of the main desorption peak are similar. Hence, we can suggest that the main hydrogen

trap in 316L SS is not dependent on the processing. However, the second trapping site of L-PBF 316L SS is stronger, compared both to its own trap and the traps of the CR specimen (Table 2). Although the value of its activation energy is very close to the one obtained by Silverstein and Eliezer [28] for the $\varepsilon/\alpha'$ martensite phase, this is probably not the case. As was mentioned previously, the amount of martensite phase is higher for the CR specimen, yet it does not act like an irreversible trapping site (Figure 6b). Therefore, the strong hydrogen trap of L-PBF 316L SS might be attributed to the dislocation cell walls of the sub-grain structure. Recently, Chen et al. [76] showed that dislocation cell walls created by severe plastic deformation in iron could act as effective hydrogen traps. Sun et al. [77] reported that the interfaces provided by the cellular sub-grain boundaries in L-PBF 316L SS are effective sink sites for helium bubbles. Since hydrogen atoms are smaller than helium, it is reasonable to suggest that these interfaces can act as hydrogen sinks too. This also contributes to the increased resistance of L-PBF 316L SS to HE. On the contrary, CR 316L SS presents only reversible traps which can supply hydrogen atoms to critical cracking locations, thus promoting hydrogen-assisted degradation.

## 5. Conclusions

This study compares the effect of hydrogen on the microstructure and hydrogen trapping characteristics of L-PBF and CR 316L SS. The main conclusions are the following:

- L-PBF 316L SS has shown better resistance to hydrogen-induced damage and hydrogen embrittlement in comparison to its conventionally produced counterpart.
- Prior to charging, CR 316L SS presented polygonal-shaped grains with a large amount of deformation twins. The microstructure of L-PBF 316L was dominated by a metastable cellular sub-grain structure and separated by melt pool boundaries.
- The hydrogenation of CR 316L SS resulted in a relatively high amount of stress-induced martensite, whereas the $\gamma \rightarrow$ martensite transformation was suppressed in L-PBF 316L SS. This is attributed to higher austenite stability and to the cellular sub-grain structure.
- Two reversible hydrogen traps were identified for CR 316L SS. The activation energy of the first trap was estimated to be $31 \pm 2$ kJ/mol and it is attributed to an elastic stress field or a dislocation core. The second trap has a higher activation energy of $44 \pm 4$ kJ/mol and is ascribed to hydrogen trapping within the $\gamma$-austenite bulk.
- L-PBF 316L SS also presented two hydrogen traps. The first one is similar to the one of CR specimen and attributed to an elastic stress field or a dislocation core. The second has a higher activation energy of $62 \pm 5$ kJ/mol and is proposed to be attributed to the dislocation cell walls of the sub-grain structure.

**Author Contributions:** P.M., validation, investigation, writing—original draft, visualization; G.B.-H., writing—review and editing, supervision; D.E., conceptualization, supervision. All authors have read and agreed to the published version of the manuscript.

**Data Availability Statement:** The raw/processed data required to reproduce these findings cannot be shared at this time as the data also forms part of an ongoing study.

**Conflicts of Interest:** The authors declare no conflict of interest.

## References

1. Davis, J.R. *ASM Specialty Handbook: Stainless Steels*; ASM International: Materials Park, OH, USA, 1994.
2. Michler, T.; San Marchi, C.; Naumann, J.; Weber, S.; Martin, M. Hydrogen environment embrittlement of stable austenitic steels. *Int. J. Hydrogen Energy* **2012**, *37*, 16231–16246. [CrossRef]
3. Matsuoka, S.; Yamabe, J.; Matsunaga, H. Criteria for determining hydrogen compatibility and the mechanisms for hydrogen-assisted, surface crack growth in austenitic stainless steels. *Eng. Fract. Mech.* **2016**, *153*, 103–127. [CrossRef]
4. San Marchi, C.; Somerday, B.P.; Tang, X.; Schiroky, G.H. Effects of alloy composition and strain hardening on tensile fracture of hydrogen-precharged type 316 stainless steels. *Int. J. Hydrogen Energy* **2008**, *33*, 889–904. [CrossRef]
5. San Marchi, C.; Somerday, B.P. *Technical Reference for Hydrogen Compatibility of Materials*; Sandia National Laboratories: Livermore, CA, USA, 2012; SAND2012-7321.

6. Perng, T.P.; Altstetter, C.J. Effects of deformation on hydrogen permeation in austenitic stainless steels. *Acta Metall.* **1986**, *34*, 1771–1781.

7. Wang, Y.; Wang, X.; Gong, J.; Shen, L.; Dong, W. Hydrogen embrittlement of catholically hydrogen-precharged 304L austenitic stainless steel: Effect of plastic pre-strain. *Int. J. Hydrogen Energy* **2014**, *39*, 13909–13918. [CrossRef]

8. Zhang, L.; Li, X.; Zheng, J.; Zhao, Y.; Xu, P.; Zhou, C.; Li, X. Effect of strain-induced martensite on hydrogen embrittlement of austenitic stainless steels investigated by combined tension and hydrogen release methods. *Int. J. Hydrogen Energy* **2013**, *38*, 8208–8214. [CrossRef]

9. Frazier, W.E. Metal additive manufacturing: A review. *J. Mater. Eng. Perform.* **2014**, *23*, 1917–1928. [CrossRef]

10. Herzog, D.; Seyda, V.; Wycisk, E.; Emmelmann, C. Additive manufacturing of metals. *Acta Mater.* **2016**, *117*, 371–392. [CrossRef]

11. DebRoy, T.; Wei, H.L.; Zuback, J.S.; Mukherjee, T.; Elmer, J.W.; Milewski, J.O.; Beese, A.M.; Wilson-Heid, A.; De, A.; Zhang, W. Additive manufacturing of metallic components–Process, structure and properties. *Prog. Mater. Sci.* **2018**, *92*, 112–224. [CrossRef]

12. Wang, Y.M.; Voisin, T.; McKeown, J.T.; Ye, J.; Calta, N.P.; Li, Z.; Zeng, Z.; Zhang, Y.; Chen, W.; Roehling, T.T.; et al. Additively manufactured hierarchical stainless steels with high strength and ductility. *Nat. Mater.* **2018**, *17*, 63–70. [CrossRef]

13. Bajaj, P.; Hariharan, A.; Kini, A.; Kürnsteiner, P.; Raabe, D.; Jägle, E.A. Steels in additive manufacturing: A review of their microstructure and properties. *Mater. Sci. Eng. A* **2020**, *772*, 138633. [CrossRef]

14. Gorsse, S.; Hutchinson, C.; Gouné, M.; Banerjee, R. Additive manufacturing of metals: A brief review of the characteristic microstructures and properties of steels, Ti-6Al-4V and high-entropy alloys. *Sci. Technol. Adv. Mater.* **2017**, *18*, 584–610. [CrossRef] [PubMed]

15. Zhong, Y.; Liu, L.; Wikman, S.; Cui, D.; Shen, Z. Intragranular cellular segregation network structure strengthening 316L stainless steel prepared by selective laser melting. *J. Nucl. Mater.* **2016**, *470*, 170–178. [CrossRef]

16. Haghdadi, N.; Laleh, M.; Moyle, M.; Primig, S. Additive manufacturing of steels: A review of achievements and challenges. *J. Mater. Sci.* **2021**, *56*, 64–107. [CrossRef]

17. Kong, D.; Dong, C.; Wei, S.; Ni, X.; Zhang, L.; Li, R.; Wang, L.; Man, C.; Li, X. About metastable cellular structure in additively manufactured austenitic stainless steels. *Addit. Manuf.* **2021**, *38*, 101804. [CrossRef]

18. Sun, Z.; Tan, X.; Tor, S.B.; Chua, C.K. Simultaneously enhanced strength and ductility for 3D-printed stainless steel 316L by selective laser melting. *NPG Asia Mater.* **2018**, *10*, 127–136. [CrossRef]

19. Liu, L.; Ding, Q.; Zhong, Y.; Zou, J.; Wu, J.; Chiu, Y.L.; Li, J.; Zhang, Z.; Yu, Q.; Shen, Z. Dislocation network in additive manufactured steel breaks strength–ductility trade-off. *Mater. Today* **2018**, *21*, 354–361. [CrossRef]

20. Voisin, T.; Forien, J.; Perron, A.; Aubry, S.; Bertin, N.; Samanta, A.; Baker, A.; Wang, Y.M. New insights on cellular structures strengthening mechanisms and thermal stability of an austenitic stainless steel fabricated by laser powder-bed-fusion. *Acta Mater.* **2021**, *203*, 116476. [CrossRef]

21. Kong, D.C.; Dong, C.F.; Ni, X.Q. Superior resistance to hydrogen damage for selective laser melted 316L stainless steel in a proton exchange membrane fuel cell environment. *Corros. Sci.* **2020**, *166*, 108425. [CrossRef]

22. Lin, J.; Chen, F.; Liu, F.; Xu, D.; Gao, J.; Tang, X. Hydrogen permeation behavior and hydrogen-induced defects in 316L stainless steels manufactured by additive manufacturing. *Mater. Chem. Phys.* **2020**, *250*, 123038. [CrossRef]

23. Khaleghifar, F.; Razeghi, K.; Heidarzadeh, A.; Taherzadeh Mousavian, R. Effect of Hydrogen on the Tensile Behavior of Austenitic Stainless Steels 316L Produced by Laser-Powder Bed Fusion. *Metals* **2021**, *11*, 586. [CrossRef]

24. Lee, D.; Sun, B.; Lee, S.; Ponge, D.; Jägle, E.A.; Raabe, D. Comparative study of hydrogen embrittlement resistance between additively and conventionally manufactured 304L austenitic stainless steels. *Mater. Sci. Eng. A* **2021**, *803*, 140499. [CrossRef]

25. Pressouyre, G.M. Trap theory of hydrogen embrittlement. *Acta Metall.* **1980**, *28*, 895–911. [CrossRef]

26. Pressouyre, G.M.; Bernstein, I.M. A kinetic trapping model for hydrogen-induced cracking. *Acta Metall.* **1979**, *27*, 89–100. [CrossRef]

27. Pressouyre, G.M. A classification of hydrogen traps in steel. *Metall. Trans. A* **1979**, *10*, 1571–1573. [CrossRef]

28. Silverstein, R.; Eliezer, D. Mechanisms of hydrogen trapping in austenitic, duplex, and super martensitic stainless steels. *J. Alloys. Compd.* **2017**, *720*, 451–459. [CrossRef]

29. Silverstein, R.; Eliezer, D.; Boellinghaus, T. Hydrogen-trapping mechanisms of TIG-welded 316L austenitic stainless steels. *J. Mater. Sci.* **2018**, *53*, 10457–10468. [CrossRef]

30. Laureys, A.; Claeys, L.; Pinson, M.; Depover, T.; Verbeken, K. Thermal desorption spectroscopy evaluation of hydrogen-induced damage and deformation-induced defects. *Mater. Sci. Technol.* **2020**, *36*, 1389–1397. [CrossRef]

31. Todoshchenko, O.; Yagodzinskyy, Y.; Hänninen, H. Thermal desorption of hydrogen from AISI 316L stainless steel and pure nickel. *Defect Diffus. Forum* **2013**, *344*, 71–77. [CrossRef]

32. Bach, A.C.; Martin, F.; Duhamel, C.; Perrin, S.; Jomard, F.; Crépin, J. Hydrogen trapping by irradiation-induced defects in 316l stainless steel. In *The Minerals, Metals & Materials Series, Proceedings of the 18th International Conference on Environmental Degradation of Materials in Nuclear Power System–Water Reactors, Portland, OR, USA, 13–17 August 2017*; Jackson, J., Paraventi, D., Wright, M., Eds.; Springer: Cham, Germany, 2019.

33. *ASTM A240/A240M-05*; Standard Specification for Chromium and Chromium-Nickel Stainless Steel Plate, Sheet, and Strip for Pressure Vessels and for General Applications. ASTM International: West Conshohocken, PA, USA, 2018.

34. *ASTM E407-07*; Standard Practice for Microetching Metals and Alloys. ASTM International: West Conshohocken, PA, USA, 2015.

35. Lee, S.; Lee, J. The trapping and transport phenomena of hydrogen in nickel. *Metall. Mater. Trans. A* **1986**, *17*, 181–187. [CrossRef]

36. Tal-Gutelmacher, E.; DEliezer, D.; Abramov, E. Thermal desorption spectroscopy (TDS)-Application in quantitative study of hydrogen evolution and trapping in crystalline and non-crystalline materials. *Mater. Sci. Eng. A* **2007**, *445–446*, 625–631. [CrossRef]

37. Metalnikov, P.; Eliezer, D.; Ben-Hamu, G. Hydrogen trapping in additive manufactured Ti–6Al–4V alloy. *Mater. Sci. Eng. A* **2021**, *811*, 141050. [CrossRef]

38. Rozenak, P.; Zevin, L.; Eliezer, D. Hydrogen effects on phase transformations in austenitic stainless steels. *Mater. Sci.* **1984**, *19*, 567–573. [CrossRef]

39. Silverstein, R.; Eliezer, D.; Glam, B.; Eliezer, S.; Moreno, D. Evaluation of hydrogen trapping mechanisms during performance of different hydrogen fugacity in a lean duplex stainless steel. *J. Alloys. Compd.* **2015**, *648*, 601–608. [CrossRef]

40. Silverstein, R.; Eliezer, D.; Tal-Gutelmacher, E. Hydrogen trapping in alloys studied by thermal desorption spectrometry. *J. Alloy. Comp.* **2018**, *747*, 511–522. [CrossRef]

41. Yagodzinskyy, Y.; Todoshchenko, O.; Papula, S. Hydrogen solubility and diffusion in austenitic stainless steels studied with thermal desorption spectroscopy. *Steel Res. Int.* **2011**, *82*, 20–25. [CrossRef]

42. Dabah, E.; Lisitsyn, V.; Eliezer, D. Performance of hydrogen trapping and phase transformation in hydrogenated duplex stainless steels. *Mater. Sci. Eng. A* **2010**, *527*, 4851–4857. [CrossRef]

43. Park, Y.; Maroef, I.; Landau, A.; Olson, D. Retained austenite as a hydrogen trap in steel welds. *Welding J.* **2002**, *81*, 27–35.

44. Gibala, R.; Kumnick, A.J. Hydrogen trapping in iron and steels. In *Hydrogen Embrittlement and Stress Corrosion Cracking*; Gibala, R., Hehermann, R.F., Eds.; ASM International: Materials Park, OH, USA, 1984; pp. 61–77.

45. Castaño-Rivera, P.C.; Ramunni, V.P.; Bruzzoni, P. Hydrogen trapping in an API 5L X60 steel. *Corros. Sci.* **2012**, *54*, 106–118. [CrossRef]

46. Turnbull, A.; Hutchings, R.B. Analysis of hydrogen atom transport in a two-phase alloy. *Mater. Sci. Eng. A* **1994**, *177*, 161–171. [CrossRef]

47. Sun, B.; Krieger, W.; Rohwerder, M.; Ponge, D.; Raabe, D. Dependence of hydrogen embrittlement mechanisms on microstructure-driven hydrogen distribution in medium Mn steels. *Acta Mater.* **2020**, *183*, 313–328. [CrossRef]

48. Pressouyre, G.M.; Bernstein, I.M. A quantitative analysis of hydrogen trapping. *Metall. Trans. A* **1978**, *9*, 1571–1580. [CrossRef]

49. Maroef, I.; Olson, D.L.; Eberhart, M.; Edwards, G.R. Hydrogen trapping in ferritic steel weld metal. *Int. Mat. Rev.* **2002**, *47*, 191–223. [CrossRef]

50. Ningshen, S.; Uhlemann, M.; Schneider, F.; Khatak, H. Diffusion behaviour of hydrogen in nitrogen containing austenitic alloys. *Corros. Sci.* **2001**, *43*, 2255–2264. [CrossRef]

51. Chun, Y.S.; Kim, J.S.; Park, K.T.; Lee, Y.K.; Lee, C.S. Role of $\varepsilon$ martensite in tensile properties and hydrogen degradation of high-Mn steels. *Mater. Sci. Eng. A* **2012**, *533*, 87–95. [CrossRef]

52. Sofinowski, K.A.; Raman, S.; Wang, X.; Gaskey, B.; Seita, M. Layer-wise engineering of grain orientation (LEGO) in laser powder bed fusion of stainless steel 316L. *Addit. Manuf.* **2021**, *38*, 101809. [CrossRef]

53. Sun, S.H.; Ishimoto, T.; Hagihara, K.; Tsutsumi, Y.; Hanawa, T.; Nakano, T. Excellent mechanical and corrosion properties of austenitic stainless steel with a unique crystallographic lamellar microstructure via selective laser melting. *Scr. Mater.* **2019**, *159*, 89–93. [CrossRef]

54. Shrinivas, V.; Varma, S.K.; Murr, L.E. Deformation-induced martensitic characteristics in 304 and 316 stainless steels during room-temperature rolling. *Metall. Trans. A* **1995**, *26*, 661–671. [CrossRef]

55. Spencer, K.; Veron, M.; Yu-Zhang, K.; Embury, J.D. The strain induced martensite transformation in austenitic stainless steels part I—influence of temperature. *Mater. Sci. Tech.* **2009**, *25*, 7–17. [CrossRef]

56. De, A.K.; Murdock, D.C.; Mataya, M.C.; Speer, J.G.; Matlock, D.K. Quantitative measurement of deformation-induced martensite in 304 stainless steel by X-ray diffraction. *Scr. Mater.* **2004**, *50*, 1445–1449. [CrossRef]

57. Yang, Q.; Luo, J.L. Martensite transformation and surface cracking of hydrogen charged and outgassed type 304 stainless steel. *Mater. Sci. Eng. A* **2000**, *288*, 75–83. [CrossRef]

58. Narita, N.; Altstetter, C.J.; Birnbaum, H.K. Hydrogen-related phase transformations in austenitic stainless steels. *Metall. Trans. A* **1982**, *13*, 1355–1365. [CrossRef]

59. Navi, N.U.; Tenenbaum, J.; Sabatani, E.; Kimmel, G.; Ben David, R.; Rosen, B.A.; Barkay, Z.; Ezersky, V.; Tiferet, E.; Ganor, Y.I.; et al. Hydrogen effects on electrochemically charged additive manufactured by electron beam melting (EBM) and wrought Ti–6Al–4V alloys. *Int. J. Hydrogen Energy* **2020**, *45*, 25523–25540. [CrossRef]

60. Louthan, M.R.; Derrick, R.G. Hydrogen transport in austenitic stainless steel. *Corros. Sci.* **1975**, *15*, 565–577. [CrossRef]

61. Du, Y.; Gao, X.H.; Du, Z.W.; Lan, L.Y.; Misra, R.D.K.; Wu, H.Y.; Du, L.X. Hydrogen Diffusivity in Different Microstructural Components in Martensite Matrix with Retained Austenite. *Int. J. Hydrogen Energy* **2021**, *46*, 8269–8284. [CrossRef]

62. Buckley, J.R.; Hardie, D. The effect of pre-straining and delta-ferrite on the embrittlement of 304L stainless steel by hydrogen. *Corros. Sci.* **1993**, *34*, 93–107. [CrossRef]

63. Rozenak, P.; Eliezer, D. Effects of ageing after cathodic charging in austenitic stainless steels. *J. Mater. Sci.* **1984**, *19*, 3873–3879. [CrossRef]

64. Rozenak, P.; Eliezer, D. Phase changes related to hydrogen-induced cracking in austenitic stainless steel. *Acta Metall.* **1987**, *35*, 2329–2340. [CrossRef]

65. Silverstein, R.; Eliezer, D. *Hydrogen Embrittlement of Duplex Stainless Steels, In Science and Technology of Polymers and Advanced Materials: Applied Research Methods*, 1st ed.; Mukbaniani, O.V., Tatrishvili, T.N., Abadie, M.J.M., Eds.; Apple Academic Press: Waretown, NJ, USA, 2019.

66. Silverstein, R.; Eliezer, D. Hydrogen trapping mechanism of different duplex stainless steels alloys. *J. Alloys. Compd.* **2015**, *644*, 280–286. [CrossRef]

67. Moshtaghi, M.; Safyari, M. Effect of work hardening mechanisms in asymmetrically cyclic loaded austenitic stainless steels on low-cycle and high-cycle fatigue behavior. *Steel Res. Int.* **2021**, *92*, 202000242. [CrossRef]

68. Glage, A.; Weidner, A.; Biermann, H. Effect of austenite stability on the low cycle fatigue behavior and microstructure of high alloyed metastable austenitic cast TRIP steels. *Procedia Eng.* **2010**, *2*, 2085–2094. [CrossRef]

69. Molnar, D.; Sun, X.; Lu, S.; Li, W.; Engberg, G.; Vitos, L. Effect of temperature on the stacking fault energy and deformation behaviour in 316L austenitic stainless steel. *Mater. Sci. Eng. A* **2019**, *759*, 490–497. [CrossRef]

70. Lo, K.H.; Shek, C.H.; Lai, J.K.L. Recent developments in stainless steels. *Mater. Sci. Eng. R* **2009**, *65*, 39–104. [CrossRef]

71. Louthan, M.R.; Caskey, G.R.; Donovan, J.A.; Rawl, D.E. Hydrogen embrittlement of metals. *Mater. Sci. Eng.* **1972**, *10*, 357–368. [CrossRef]

72. Angel, T.J. Formation of martensite in austenitic stainless steels. *J. Iron Steel Inst.* **1954**, *177*, 165–174.

73. Yonezawa, T.; Suzuki, K.; Ooki, S.; Hashimoto, A. The effect of chemical composition and heat treatment conditions on stacking fault energy for Fe-Cr-Ni austenitic stainless steel. *Metall. Mater. Trans. A* **2013**, *44*, 5884–5896. [CrossRef]

74. Hong, Y.J.; Zhou, C.S.; Zheng, Y.Y.; Zhang, L.; Zheng, J.Y.; Chen, X.Y.; An, B. Formation of strain-induced martensite in selective laser melting austenitic stainless steel. *Mater. Sci. Eng. A* **2019**, *740-741*, 420–426. [CrossRef]

75. Dayal, R.K.; Parvathavarthini, N. Hydrogen embrittlement in power plant steels. *Sadhana* **2003**, *28*, 431–451. [CrossRef]

76. Chen, L.; Xiong, X.; Tao, X.; Su, Y.; Qiao, L. Effect of dislocation cell walls on hydrogen adsorption, hydrogen trapping and hydrogen embrittlement resistance. *Corros. Sci.* **2020**, *166*, 108428. [CrossRef]

77. Sun, X.Y.; Chen, F.D.; Huang, H.; Lin, J.W.; Tang, X.B. Effects of interfaces on the helium bubble formation and radiation hardening of an austenitic stainless steel achieved by additive manufacturing. *Appl. Surf. Sci.* **2019**, *467*, 1134–1139. [CrossRef]